Nonlinear Dyn (2017) 89:1525–1538
DOI 10.1007/s11071-017-3532-z

ORIGINAL PAPER

# Dynamic behavior of an electrostatic MEMS resonator with repulsive actuation

**Mark Pallay** · **Meysam Daeichin** · **Shahrzad Towfighian**

Received: 29 August 2016 / Accepted: 11 April 2017 / Published online: 24 April 2017
© Springer Science+Business Media Dordrecht 2017

**Abstract** Static and dynamic analyses of an electrostatic microbeam under repulsive force actuation are presented. The repulsive force, created through a specific electrode configuration, generates a net electrostatic force on the beam pushing it away from the substrate. This allows large out-of-plane actuation and eliminates the pull-in instability. For example, a dynamic amplitude of 15 μm was recorded for a 500-μm-long cantilever at a DC voltage of 195 V and an AC voltage of 1 V, while the initial gap was only 2 μm. This study includes mathematical modeling and simulations for a cantilever and a clamped–clamped beam, as well as experimental validation. The beam is modeled using Euler–Bernoulli beam theory and electromechanical coupling effects. Cantilever tip displacement, clamped–clamped midpoint deflection, and natural frequency shifts are reported. Governing equations are solved numerically using the shooting method, which provides a complete picture of the beam dynamics. The numerical results are verified with experimental data from fabricated beams using PolyMUMPs standard fabrication. Frequency response results reveal a mixed softening and hardening behavior and secondary resonances originating from quadratic and cubic nonlinearities in the governing equations. The analysis provides insight for applications in optical and gas sensors where a large signal-to-noise ratio and, sometimes, a wide frequency bandwidth are desired.

**Keywords** MEMS resonators · Repulsive force actuation · Electrostatic · Nonlinear dynamics · Secondary resonances

M. Pallay · M. Daeichin · S. Towfighian (✉)
State University of New York at Binghamton,
4400 Vestal Parkway East, Binghamton, NY 13902, USA
e-mail: stowfigh@binghamton.edu

M. Daeichin
e-mail: mdaeich1@binghamton.edu

M. Pallay
e-mail: mpallay1@binghamton.edu

## 1 Introduction

Micro-electromechanical systems (MEMS) are now widespread in the automotive, medical, and cell phone industries. MEMS resonators are a class of MEMS devices used extensively in sensing [1–7], energy harvesting [8–11], signal filtering [12–14], and many other applications [15–18]. The most popular actuation mechanism for MEMS resonators uses the electrostatic force because it consumes little power and is easy to fabricate. Because of this, many electrostatic actuator designs have been investigated and applied to electronic devices in use today [1–7,12,15–18]. The most common configuration for electrostatic actuators is parallel plates. The two main drawbacks associated with parallel-plate electrodes are pull-in instability and limited travel ranges. Pull-in occurs when the attractive electrostatic force between electrodes becomes so large that it overcomes the mechanical restoring forces causing the collapse of the moving electrode. This is desir-

able in some applications, such as switches [19], but can be devastating in other applications such as resonators [20]. There is a need for new actuator designs that can overcome the severe limitations of parallel-plate actuators. However, new designs cannot find proper applications without careful investigations of their highly nonlinear behavior that stems from the electrostatic force.

The nonlinear dynamic behavior of electrostatic MEMS resonators has been studied extensively [21–27] for various applications. Braghin et al. [21] looked at nonlinear hardening behavior in a MEMS comb-drive resonator to increase the sensibility of MEMS gyroscopes. Younis et al. [23] studied the nonlinear dynamic response of an electrostatically actuated MEMS arch with softening, hardening, hysteresis, dynamic pull-in, and snap-through, for use in bandpass filters. Towfighian et al. [24] studied microbeam resonators with chaotic responses. Ozdogan and Towfighian [25] investigated the nonlinear dynamics of a MEMS torsional micromirror with softening effects and secondary resonances for use in optical applications.

Some effort has been put into creating repulsive electrostatic actuation, where the actuator is pushed away from the electrode [28–31]. This eliminates the risk of pull-in and allows for much higher actuation amplitudes. A repulsive electrostatic actuator can be achieved in several ways.

As originally reported by Lee and Cho [28], a net repulsive force is created between two grounded electrodes if they are placed between two charged electrodes. As mentioned in [31], the force on the movable electrode is not a repelling force from the fixed, grounded electrode, but rather a net attractive force away from the substrate because of the presence of the charged electrodes on the sides.

A different approach was taken by Shen and Kan [29], who created a repulsive force by charging two beams to the same polarity through hot-electron injection. This is a true repulsive force. However, the charge on the beams decayed quickly (even though some charge would remain for a long time) and much of the actuation power was lost after a few minutes. Sugimoto et al. [31] used this principle to create a repulsive actuation force. In this design, the beam was periodically charged through electrostatic induction rather than hot-electron injection. Induction creates attractive electrostatic forces as well; thus, this design is susceptible to pull-in during certain phases of operation.

He and Ben Mrad [30] designed a repulsive force actuator for out-of-plane motion where two grounded electrodes are placed between two charged electrodes. Unlike in-plane actuation, by Lee and Cho [28], this design can produce out-of-plane actuation for use in micromirrors. A major advantage of this design is its simplicity and ease of fabrication with the PolyMUMPs standard. This design could also be used in multiple layers to create even larger actuation amplitudes [32]. Improvements, optimizations, and other applications of this design have been reported [32–37].

To the best of our knowledge, all efforts on repulsive force actuators have been put into studying the repulsive force and its influence on the static behavior of the actuators. As many repulsive force actuators can be used in resonant modes, more fundamental studies on the dynamic response of these actuators are notably needed. The contribution of this paper is to investigate the static and dynamic performance of repulsive force actuators in cantilever and clamped–clamped configurations. For the first time, we have demonstrated for repulsive force actuators the effect of nonlinear repulsive force on the shifting of natural frequency and frequency softening and hardening. As pull-in does not occur, this mechanism is very attractive for MEMS resonators, such as low-pressure sensors and optical devices such as micromirrors and polychromators, that require large out-of-plane actuation. The numerical shooting method is used to solve governing equations of motion, and the results are verified through experiment. The shooting method is computationally efficient and provides a fundamental understanding of the electrostatic beam dynamics under repulsive force.

The repulsive force actuator is shown in Fig. 1 with dimensions and properties given in Table 1. The electrode configuration is adapted from He and Ben Mrad [30] to produce out-of-plane actuation. It consists of

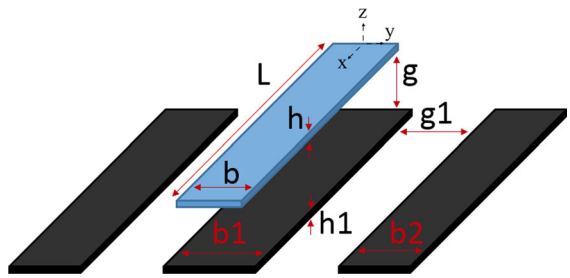


**Fig. 1** Layout of the repulsive force actuator. The *blue* beam is movable and the others are fixed. (Color figure online)

**Table 1** Beam material and geometric properties

| Parameter | Symbol | Value |
|---|---|---|
| Cantilever length (μm) | $L$ | 503 |
| Clamped–clamped length (μm) | $L$ | 1000 |
| Beam width (μm) | $b$ | 17.5 |
| Beam height (μm) | $h$ | 2 |
| Beam–electrode gap (μm) | $g$ | 2 |
| Electrode gap (μm) | $g1$ | 20.5 |
| Electrode width 1 (μm) | $b1$ | 30 |
| Electrode width 2 (μm) | $b2$ | 28 |
| Electrode thickness (μm) | $h1$ | 0.5 |
| Elastic modulus (GPa) | $E$ | 150 |
| Density (kg/m$^3$) | $\rho$ | 2330 |
| Poisson's ratio | $v$ | 0.22 |
| Force constant | $p_5$ | $-8.5695 \times 10^{14}$ |
| Force constant | $p_4$ | $1.7347 \times 10^{11}$ |
| Force constant | $p_3$ | $-1.2595 \times 10^{7}$ |
| Force constant | $p_2$ | $3.5574 \times 10^{2}$ |
| Force constant | $p_1$ | $-3.8677 \times 10^{-4}$ |
| Force constant | $p_0$ | $-1.1703 \times 10^{-7}$ |

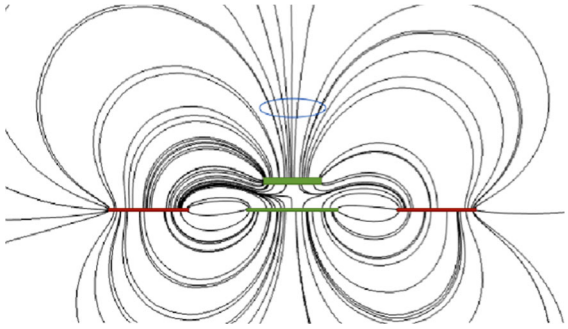

**Fig. 2** Electric field lines for the actuator. Charged electrodes are highlighted in *red* and grounded electrodes (including beam) are highlighted in *green*. *Blue ellipse* shows the approximate location of the equilibrium point. (Color figure online)

a beam suspended above three fixed electrodes on the substrate. The beam and center electrode are grounded, while the side electrodes are charged. When a charge is applied to the side electrodes an electric field is produced (Fig. 2). Under the influence of the electric field, the beam wants to move to some equilibrium point away from the substrate. The location of this equilibrium point is directly above the center electrode at a distance that is highly dependent on the geometry of the electrodes. For a beam with the dimensions given in Table 1, the equilibrium position is located at an approximate height of 60 microns. If the beam is placed less than 60 microns away from the center electrode, it will experience a net force away from the electrodes and it will be pulled toward the substrate if the distance is greater than 60 microns.

The outline of this paper is as follows. Section 2 outlines the theoretical model derivation. Section 3.1 shows the static and dynamic analyses for the cantilever beam and Sect. 3.2 for the clamped–clamped beam. The conclusions based on the analyses are given in Sect. 4.

## 2 Model derivation

The beam is modeled using Euler–Bernoulli beam theory with mid-plane stretching. The beam material is polysilicon with dimensions and material properties given in Table 1. We assume negligible axial and in-plane transverse displacement, as well as no twisting of the beam. Thus, we only consider out-of-plane deflection as a function of beam position and time. The governing equation of motion is given as,

$$\rho A \frac{\partial^2 \hat{w}}{\partial \hat{t}^2} + \hat{c}\frac{\partial \hat{w}}{\partial \hat{t}} + \gamma \frac{EA}{2L}\frac{\partial^2 \hat{w}}{\partial \hat{x}^2}\int_0^L \left(\frac{\partial \hat{w}}{\partial \hat{x}}\right)^2 \mathrm{d}x + EI\frac{\partial^4 \hat{w}}{\partial \hat{x}^4} + \hat{f}_e(\hat{w})V^2 = 0 \tag{1}$$

In Eq. (1), $\hat{w}$ is the $z$-direction beam displacement, $I$ is the moment of inertia, $V$ is the electrode voltage, $\hat{f}_e$ is the electrostatic force, and $\gamma$ indicates the mid-plane stretching effect. $\gamma$ is $-1$ for the clamped–clamped beam and 0 for the cantilever [38]. To find the repulsive electrostatic force profile, a finite element simulation in COMSOL was conducted for the fabricated dimensions (Fig. 3). A 5th-order polynomial is fit to the numerical force profile to be used in Eq. (1).

Because of the small scale of the beams, a non-dimensional form of Eq. (1) is used. The non-dimensional substitutions and parameters are shown in Table 2 and the non-dimensional equation of motion is given as

$$\frac{\partial^2 w}{\partial t^2} + c\frac{\partial w}{\partial t} + \gamma r_1 \frac{\partial^2 w}{\partial x^2}\int_0^1 \left(\frac{\partial w}{\partial x}\right)^2 \mathrm{d}x + \frac{\partial^4 w}{\partial x^4} + r_2 V^2 \sum_{j=0}^{5} p_j h^j w^j = 0 \tag{2}$$

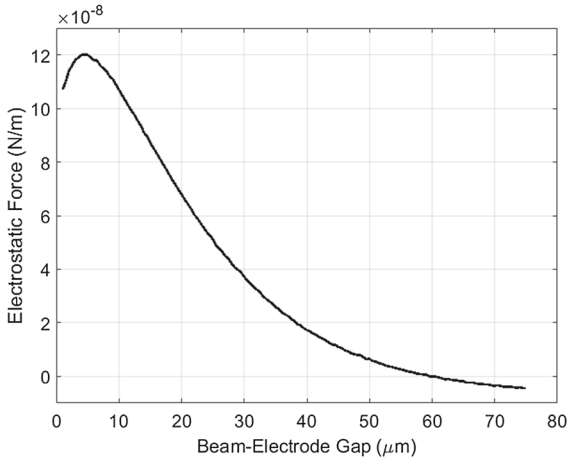


**Fig. 3** Electrostatic force profile for the beam–electrode configuration shown in Fig. 1 as determined in COMSOL. Equilibrium point at 60 microns for the geometry given in Table 1

**Table 2** Non-dimensionalization

| Parameter | Substitution |
|---|---|
| $x$-direction position | $x = \hat{x}/L$ |
| $z$-direction position | $w = \hat{w}/h$ |
| Time | $t = \hat{t}/T$ |
| Damping | $c = \hat{c}L^4/EIT$ |
| Time constant | $T = \sqrt{\rho AL^4/EI}$ |
| Mid-plane stretching constant | $r_1 = Ah^2/2IL$ |
| Force constant | $r_2 = L^4/EIh$ |

where $p_j$ are constants from the 5th-order polynomial forcing profile fit. In Table 2 and Eq. (2), the non-accented variables refer to the non-dimensional quantities. Equation (2) is then discretized using Galerkin's method. The deflection of the beam is approximated as

$$w(x,t) \approx \sum_{i=1}^{n} q_i(t)\phi_i(x) \tag{3}$$

where $\phi_i(x)$ are the linear mode shapes of the beam, $q_i(t)$ are the time-dependent generalized coordinates, and $n$ is the number of degrees of freedom (DOF) to be considered. In our case, the mode shapes for a cantilever (CL) and clamped–clamped (CC) microbeam are well known and are of the form

$$\phi_i(x) = \cosh(\alpha_i x) - \cos(\alpha_i x) - \sigma_i(\sinh(\alpha_i x) - \sin(\alpha_i x)) \tag{4}$$

**Table 3** Mode shape natural frequencies and constants

| Mode | $\alpha^2$ (CL) | $\sigma_i$ (CL) | $\alpha^2$ (CC) | $\sigma_i$ (CC) |
|---|---|---|---|---|
| 1 | 3.516 | 0.7341 | 22.3733 | 0.9825 |
| 2 | 22.035 | 1.0185 | 61.6728 | 1.00078 |
| 3 | 61.697 | 0.9992 | 120.903 | 0.999966 |
| 4 | 120.904 | 1.0 | 199.859 | 1.0 |

where $\alpha_i$ are the square roots of the non-dimensional natural frequencies, and $\sigma_i$ are constants determined from the boundary conditions and mode to be considered. Values of $\alpha_i$ and $\sigma_i$ for the first four modes are obtained from [39] and are shown in Table 3.

Once the mode shapes are known, Eq. (2) becomes a coupled set of ordinary differential equations (ODE) in time for $q_i(t)$. Multiplying through by $\phi_k$ and integrating between 0 and 1 decouples the linear terms because of the orthogonality of the mode shapes and results in a set of ODEs shown in Eq. (5), coupled through the nonlinear forcing terms.

$$m_i\ddot{q}_i + cm_i\dot{q}_i + \gamma r_1 s_i + k_i q_i + r_2 V^2 \sum_{j=0}^{5} f_{ijk} q_i^j = 0 \tag{5}$$

where

$$m_i = \int_0^1 (\phi_i)^2 \mathrm{d}x \qquad k_i = \alpha_i^4 \int_0^1 (\phi_i)^2 \mathrm{d}x$$

$$s_i = \int_0^1 \phi_k \frac{\mathrm{d}^2\phi_i}{\mathrm{d}x^2} q_i \left( \int_0^1 \left( \sum_{i=1}^{n} \frac{\mathrm{d}\phi_i}{\mathrm{d}x} q_i \right)^2 \mathrm{d}x \right) \mathrm{d}x$$

$$f_{ijk} = \int_0^1 p_j h^j \phi_i^j \phi_k \mathrm{d}x$$

For a one-mode approximation, Eq. (5) reduces to,

$$m_1\ddot{q}_1 + cm_1\dot{q}_1 + \gamma r_1 \beta q_1^3 + k_1 q_1 + r_2 V^2 \sum_{j=0}^{5} \left( \int_0^1 p_j h^j \phi_1^{j+1} \mathrm{d}x \right) q_1^j = 0 \tag{6}$$

where

$$\beta = \int_0^1 \phi_1 \frac{\mathrm{d}^2\phi_1}{\mathrm{d}x^2} \left( \int_0^1 \left( \frac{\mathrm{d}\phi_1}{\mathrm{d}x} \right)^2 \mathrm{d}x \right) \mathrm{d}x$$

As it can be seen in Eq. (6), the mid-plane stretching term adds cubic nonlinearity to the system and the

repulsive force adds a polynomial of order 5. To solve the governing equation of motion, we used the shooting method. This method is computationally more efficient than direct integration and can find unstable solutions.

## 3 Results and discussion

### 3.1 Cantilever beam

For the case of a cantilever, the effect of mid-plane stretching is small. Therefore, $\gamma$ is set to 0. The boundary conditions are given as,

$$\phi(x=0)=0 \qquad \frac{\mathrm{d}\phi}{\mathrm{d}x}(x=0)=0$$
$$\frac{\mathrm{d}^2\phi}{\mathrm{d}x^2}(x=1)=0 \qquad \frac{\mathrm{d}^3\phi}{\mathrm{d}x^3}(x=1)=0 \tag{7}$$

#### *3.1.1 Static analysis*

First, the static equation is solved. The time-dependent components from Eq. (2) are removed, which results in,

$$\frac{\mathrm{d}^4 w}{\mathrm{d}x^4} + r_2 V_{\mathrm{DC}}^2 \sum_{j=0}^{5} p_j h^j w^j = 0 \tag{8}$$

Equation (8) is a boundary value problem that can be solved in numerous ways. We reduced it to four 1st-order ODEs and solved them numerically using bvp4c in MATLAB. This gives the beam profile for a given DC voltage. The tip deflection is then calculated for increasing DC voltages to capture the static solution shown in Fig. 4.

Figure 4 shows the static tip deflection for DC voltages up to 200 V. A saturation in the displacement will occur where the electrostatic force becomes attractive at approximately 60 microns. However, to reach the saturation point, a huge voltage is required, which is impractical and not shown here. For our dynamic case studies, we set the DC voltage limit to 200 V. Around this voltage, saturation is not an issue and the static solution is approximately linear.

#### *3.1.2 Dynamic numerical results*

To gain insight into the dynamic behavior, the variations of natural frequencies by the DC voltages are

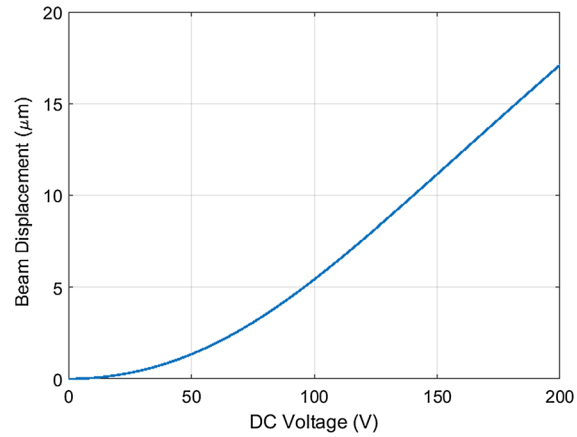


**Fig. 4** Static response of the cantilever beam tip as the DC voltage varies

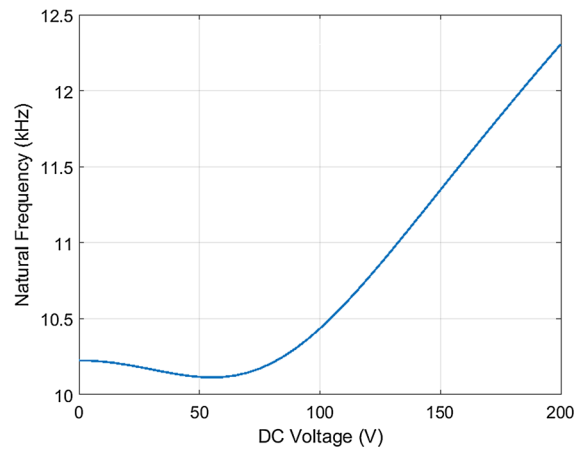


**Fig. 5** First natural frequency of the cantilever beam as the DC voltage varies

obtained. The Jacobian of Equation (5) is computed at the static equilibrium points from Fig. 4. The corresponding eigenvalues of the Jacobian yield the natural frequencies as shown in Fig. 5 using a one-mode approximation.

Unlike parallel-plate capacitors that experience a decrease in natural frequency because of an increase in the DC voltage [38], the natural frequency of the repulsive force actuator increases as the DC voltage is increased. However, the increase in natural frequency doesn't occur until about 70 VDC, at which point it increases linearly. At 200 V, the natural frequency increases by about 20%. The eigenvalues of the Jacobian also indicate whether the static solution is stable.

In this case, the real part of the eigenvalues for all solutions are negative, indicating stable solutions.

To find the dynamic response of the cantilever beam to a DC voltage superimposed by an AC voltage excitation, Eq. (5) is solved using shooting techniques outlined in [38] and then verified using long-time integration with higher modes. A one-mode approximation is used for the shooting method. First, the non-dimensional equation of motion is rewritten in state-space form,

$$\begin{cases} \dot{y}_1 = y_2 \\ \dot{y}_2 = -r_2 V^2 \sum_{j=0}^{5} \left( \int_0^1 p_j h^j \phi_1^{j+1} \mathrm{d}x \right) y_1^j - c y_2 \\ \qquad -\gamma r_1 \int_0^1 \phi_1 \frac{\mathrm{d}^2 \phi_1}{\mathrm{d}x^2} y_1 \left( \int_0^1 \left( \frac{\mathrm{d}\phi_1}{\mathrm{d}x} y_1 \right)^2 \mathrm{d}x \right) \mathrm{d}x - \omega_\mathrm{n}^2 y_1 \end{cases}$$

where $\omega_n$ is the first non-dimensional mechanical natural frequency, which can be found in Table 3. It should be noted that in the above equation, $\gamma = 0$ for the cantilever beam and $\gamma = -1$ for the clamped–clamped beam. Four new variables are defined to help find the initial conditions to capture the steady-state response.

$$y_3 = \frac{\partial y_1}{\partial \eta_1} \qquad y_4 = \frac{\partial y_1}{\partial \eta_2} \qquad y_5 = \frac{\partial y_2}{\partial \eta_1} \qquad y_6 = \frac{\partial y_2}{\partial \eta_2}$$

where $\eta_1$ is the initial displacement and $\eta_2$ is the initial velocity. Including the newly defined variables, the state-space equations become:

$$\begin{cases} \dot{y}_1 = y_2 \\ \dot{y}_2 = -r_2 V^2 \sum_{j=0}^{5} \left( \int_0^1 p_j h^j \phi_1^{j+1} \mathrm{d}x \right) y_1^j - c y_2 \\ \qquad -\gamma r_1 \left( \int_0^1 \phi_1 \frac{\mathrm{d}^2 \phi_1}{\mathrm{d}x^2} \left( \int_0^1 \left( \frac{\mathrm{d}\phi_1}{\mathrm{d}x} \right)^2 \mathrm{d}x \right) \mathrm{d}x \right) y_1^3 - \omega_\mathrm{n}^2 y_1 \\ \dot{y}_3 = y_5 \\ \dot{y}_4 = y_6 \\ \dot{y}_5 = -r_2 V^2 \sum_{j=1}^{5} \left( \int_0^1 j p_j h^j \phi_1^{j+1} \mathrm{d}x \right) y_1^{j-1} y_3 - c y_5 \\ \qquad -3\gamma r_1 \left( \int_0^1 \phi_1 \frac{\mathrm{d}^2 \phi_1}{\mathrm{d}x^2} \left( \int_0^1 \left( \frac{\mathrm{d}\phi_1}{\mathrm{d}x} \right)^2 \mathrm{d}x \right) \mathrm{d}x \right) y_1^2 y_3 - \omega_\mathrm{n}^2 y_3 \\ \dot{y}_6 = -r_2 V^2 \sum_{j=1}^{5} \left( \int_0^1 j p_j h^j \phi_1^{j+1} \mathrm{d}x \right) y_1^{j-1} y_4 - c y_6 \\ \qquad -3\gamma r_1 \left( \int_0^1 \phi_1 \frac{\mathrm{d}^2 \phi_1}{\mathrm{d}x^2} \left( \int_0^1 \left( \frac{\mathrm{d}\phi_1}{\mathrm{d}x} \right)^2 \mathrm{d}x \right) \mathrm{d}x \right) y_1^2 y_4 - \omega_\mathrm{n}^2 y_4 \end{cases}$$

They are integrated over one period ($T$) using ode45 in MATLAB with the initial conditions shown below.

$$y(0) = [\eta_1 \quad \eta_2 \quad 1 \quad 0 \quad 0 \quad 1]$$

To determine the approximate error in the initial conditions, $\partial \eta_i$, the results for $y$ at time $T$ are used in the following equation,

$$\begin{Bmatrix} \partial \eta_1 \\ \partial \eta_2 \end{Bmatrix} = \left[ \begin{Bmatrix} y_3(T) & y_4(T) \\ y_5(T) & y_6(T) \end{Bmatrix} - \begin{Bmatrix} 1 & 0 \\ 0 & 1 \end{Bmatrix} \right]^{-1} \begin{Bmatrix} \eta_1 - y_1(T) \\ \eta_2 - y_2(T) \end{Bmatrix}$$

The initial conditions are then corrected with using the approximate error.

$$y = [\eta_1 + \partial \eta_1 \quad \eta_2 + \partial \eta_2 \quad 1 \quad 0 \quad 0 \quad 1]$$

This process is repeated until the errors are sufficiently small and the results for $y_1$ and $y_2$ converge. To analyze the stability of the solution, the monodromy matrix is constructed.

$$\begin{bmatrix} y_3(T) & y_4(T) \\ y_5(T) & y_6(T) \end{bmatrix}$$

The eigenvalues of the monodromy matrix (Floquet multipliers) show whether the solution is stable. Floquet multipliers outside the unity circle in the complex plane indicate an unstable solution while inside the unity circle indicate stable solutions [40].

Damping of the system is estimated using the quality factor and the following relation:

$$c = \frac{\lambda_1^2}{Q} \tag{9}$$

where $\lambda_1^2$ is the first natural frequency of the cantilever. The quality factor in a vacuum was found to be approximately 130 in our experiment. Figure 6 demonstrates the frequency response at various AC voltages for a DC voltage of 195 V.

Dynamic responses show softening behavior and bandwidth expansion as the AC excitation increases. The bandwidth increase is desired in resonators as it contributes to a larger signal-to-noise ratio over a broader range of frequency. It should be noted that to stay on the large energy orbit in the multiple-solution region, one should use the backward sweep because of the hysteresis effect. The hysteresis and softening effect is because of a quadratic term and a negative cubic term of the electrostatic force from the forcing profile polynomial fit (refer to coefficients of $p_2$ and $p_3$ in Table 1). These two terms are the dominant terms in the forcing function, which explains why the softening is significant even at AC voltages under 1 V. Unlike long-time integration, the applied shooting method can capture the unstable solutions and is computationally much more efficient. To verify the shooting method

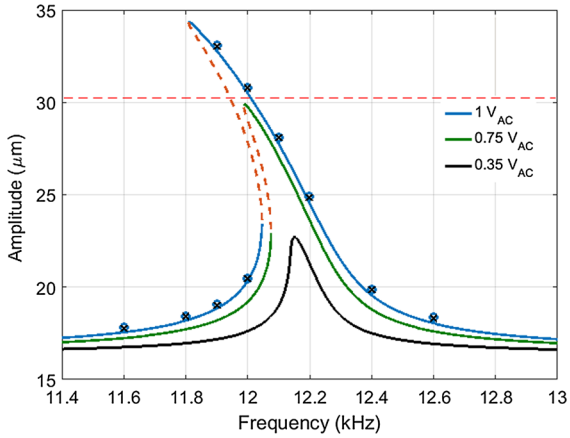


**Fig. 6** Frequency response at $V_{DC} = 195\,V$ for various AC voltages. *Dashed portions of the frequency curve* indicate unstable solutions. *Markers* indicate long-time integration results for two-mode (*times*) and three-mode (*open circle*) approximations solved with long-time integration. The *dashed red line* indicates the approximate threshold amplitude at which the beam tip will hit the substrate

results and the accuracy of a one-mode approximation, we conducted the long-time integration on several points for two- and three-mode models as depicted by markers in Fig. 6. Convergence of the results is obtained after at least three modes are considered, though a one-mode model provides a very accurate approximation. The first mode shape is dominant because of the type of excitation that applies electrostatic force on the full electrode. A recent study has shown the use of partial electrodes can be used to excite other modes of interest [41]. We verified this assumption comparing our simulation with experimental results in Sect. 3.1.3.

It is noted that a major limiting factor for the amplitude of the AC voltage is the small gap between the beam and the center electrode. If the AC voltage is too high, the beam will hit the bottom electrode, which affects the response of the beam and should be avoided. The approximate amplitude at which this occurs (the threshold amplitude) is shown in the frequency response plots with the dashed red line. To accurately draw this line, we also assured that transients at threshold frequencies do not hit the substrate either. As an approximate rule of thumb, the maximum total deflection can reach roughly twice the static deflection before the beam begins to hit the electrode. For example, if the static deflection is $10\,\mu m$, the maximum deflection the beam can experience is approximately $20\,\mu m$ before a collision with the bottom electrode will occur. To partially mitigate this issue, the DC voltage can be increased as the maximum amplitude at which the beam can reach before hitting the substrate is determined by the DC voltage. The increase in DC voltage moves the static equilibrium away from the electrodes, which allows for higher AC voltage and higher bandwidth. On the other hand, the maximum AC voltage is highly dependent on the damping of the system. High damping cases require significantly higher AC voltages to provide a wider frequency bandwidth. With the current parameters, the bandwidth is approximately 300 Hz with the maximum amplitude of about $30\,\mu m$ at $V_{DC} = 195\,V$ and $V_{AC} = 0.75\,V$ (Fig. 6).

### *3.1.3 Experimental results*

The cantilever beams were then fabricated using POLYMUMPs standard fabrication. A picture of a beam can be seen in Fig. 7. Beam imaging and static experiments were conducted using a Wyko NT1100 optical profiler. As the beams were $500\,\mu m$ long, there was some slight deformation and sagging near the beam tip of about $1–2\,\mu m$. While this would interfere slightly with the static measurement, it had negligible effects on the dynamics of the beam because of its large length. For the static test, DC voltages up to 200 V were applied. Figure 8 shows the comparison between the simulation and experiment for static tip deflection showing relatively close agreement.

The discrepancy between the static measurement and theoretical results in Fig. 8 can be mostly explained by fabrication imperfections. Close to the tip of the beam, there was a dimple that was interfering with measurements and there was a slight sagging of the beam. The location of the measurement is approximately $50\,\mu m$ from the tip of the beam to avoid the sagging and dimples as much as possible. It is impossible to avoid this entirely, so the measurement location was chosen to minimize this effect while still being near the tip of the beam. Because of these differences, the

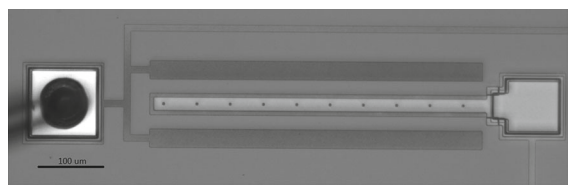


**Fig. 7** Optical profiler view of a fabricated beam

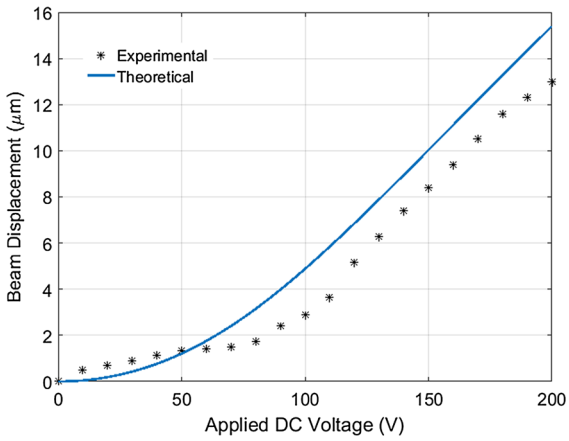


**Fig. 8** Static beam displacement versus applied DC voltage. The location of the measurement is approximately 50 μm from the tip of the beam for both the static experiment and for the theoretical model

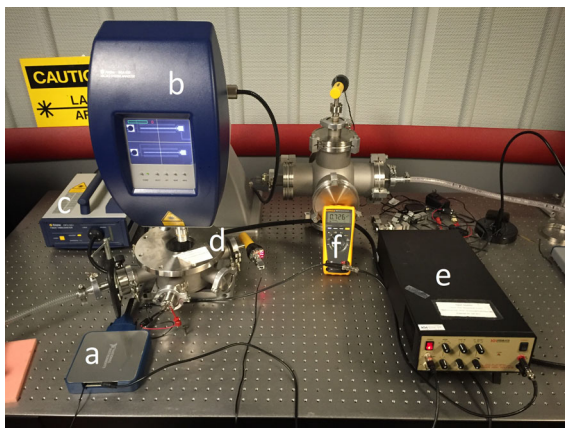


**Fig. 9** Experimental setup for dynamic testing. *a* National instruments USB 6366 data aquisition, *b* polytec MSA optical microscope, *c* polytec MSA laser, *d* vacuum chamber, *e* Krohn-Hite 7600 wideband power amplifier, *f* fluke RMS multimeter

actual deflection is slightly lower than the theoretical displacement.

To find the natural frequencies, a Polytec MSA-500 laser vibrometer was used to take velocity measurements. The dynamic experimental setup is shown in Fig. 9. The beams were placed in a vacuum chamber, and the pressure was reduced to approximately 900 mtorr. A white noise signal was applied to the electrodes, and a fast Fourier transformation was applied to the signal to find the natural frequencies. A comparison between the fundamental natural frequency from the experiment and simulation can be seen in Fig. 10.

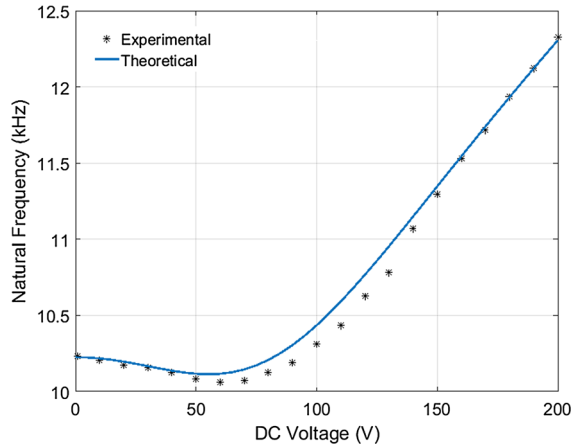


**Fig. 10** Change in experimental and theoretical natural frequencies with applied DC voltage

There is a slight discrepancy between the simulation and experimental natural frequencies (Fig. 10). This is most likely from the dimples, which were placed along the bottom of the beam to prevent them from sticking to the substrate. This may cause the actual electrostatic force profile to vary slightly because the dimples are closer to the substrate than the actual beam, which would result in a larger electrostatic force. This could explain why the effect of the electrostatic force on the reduction of the natural frequency is slightly greater in the experiment. This discrepancy fades away for voltages above 150 V because of the large distance from the bottom electrode that makes the effect of dimples negligible.

Lastly, frequency sweeps were conducted to verify the softening behavior seen in the numerical model. The data acquisition was performed using the MATLAB DAQ toolbox. Several important factors needed to be considered during the dynamic experiment. As mentioned above, the DC voltage needs to be high enough so that the beam has room to vibrate without hitting the substrate. Also, because of noise in the electrical signal at low AC voltages, the pressure was adjusted so that 1 $V_{AC}$ could be used without hitting the substrate, while still showing nonlinearity. A pressure and DC voltage of 900 mtorr and 195 V, respectively, were used in the frequency sweep. For this measurement, beam velocity was recorded at around 50 μm from the tip. Then, a sine curve was fit to the data to eliminate signal noise using the method of least squares. Finally, the velocity was converted to dynamic displacement by dividing the velocity signal by the frequency. Figure 11 shows the experimental dynamic frequency response.

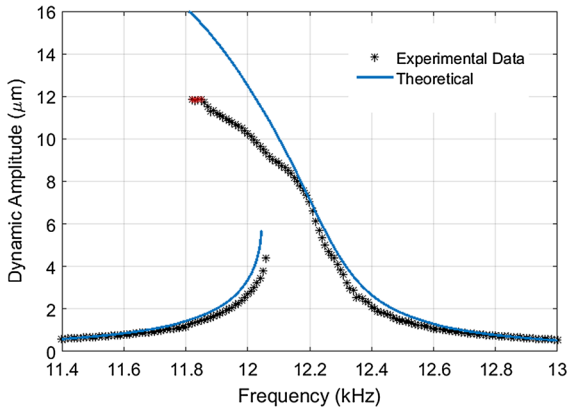


**Fig. 11** Dynamic frequency response at $V_{DC} = 195\,\text{V}$, $V_{AC} = 1\,\text{V}$ and a vacuum pressure of 900 mtorr. A quality factor of 130 was used for the theoretical model. The velocity measurement was taken from about 50 μm from the tip of the beam. Highlighted *red markers* show points where the beam hits the electrode. (Color figure online)

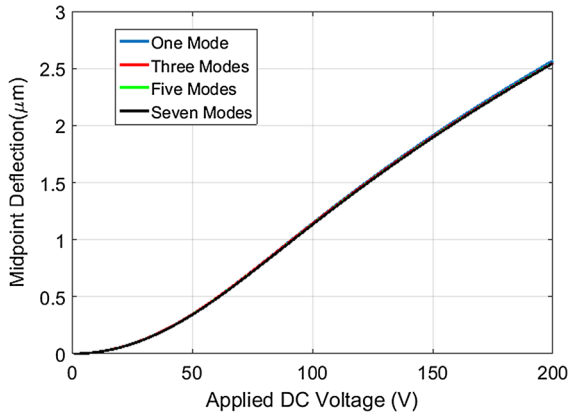


**Fig. 12** Static equilibrium position of the midpoint of the clamped–clamped beam as the DC voltage varies

There is good agreement between the theoretical model and experimental frequencies response data. There is a discrepancy in the resonant peak amplitude, which is smaller in the experiment. This is most likely because of squeeze film damping, which is not accounted for in the theoretical model, but becomes noticeable when the beam gets close to the electrode. Figure 11 shows the squeeze film damping effect starts to occur right before the beam hits the electrode (highlighted points in red). The experiment also verifies the softening behavior of the electrostatic force.

### 3.2 Clamped–clamped

Next, a clamped–clamped beam is considered. Unlike a cantilever beam, mid-plane stretching has a significant effect on the dynamics of a clamped–clamped beam. Therefore, $\gamma$ is set to $-1$ in Eq. (5) to include the mid-plane stretching term. The beam length used for the simulation is 1000 μm. The boundary conditions for a clamped–clamped beam are

$$\begin{aligned} \phi(x=0) &= 0 \qquad \frac{\mathrm{d}^2\phi}{\mathrm{d}x^2}(x=0) = 0 \\ \phi(x=1) &= 0 \qquad \frac{\mathrm{d}^2\phi}{\mathrm{d}x^2}(x=1) = 0 \end{aligned} \tag{10}$$

#### *3.2.1 Static analysis*

First, the static equilibrium equation for the clamped–clamped beam is given as

$$\frac{\mathrm{d}^4 w}{\mathrm{d}x^4} + r_1 \frac{\mathrm{d}^2 w}{\mathrm{d}x^2} \int_0^1 \left(\frac{\mathrm{d}w}{\mathrm{d}x}\right)^2 \mathrm{d}x + r_2 V_{DC}^2 \sum_{j=0}^{5} p_j h^j w^j = 0 \tag{11}$$

To solve this equation, we plug in the Galerkin expansion [Eq. (3)] using up to a four-mode approximation (excluding non-symmetric modes) and solve with MATLAB. This yields the beam profile as a function of applied DC voltage. Then, we can calculate the maximum deflection, shown in Fig. 12, which occurs at the midpoint of the beam because of its symmetry. It is worth mentioning that because of this symmetry, only symmetric mode shapes of a clamped–clamped beam (i.e., mode 1, 3, 5, 7) are considered [42]. We can see that a one-mode approximation can catch the response of the beam with good accuracy. Unlike a conventional parallel-plate clamped–clamped beam that takes a convex shape under applied voltage, the repulsive force beam takes a concave shape, which allows for a higher displacement range than the initial gap. The mid-plane stretching effect and a more restricted boundary condition significantly limit the maximum amplitude, and inhibit saturation compared to the cantilever case.

#### *3.2.2 Dynamic numerical results*

Next, the time-dependent components are added back into the governing equation to determine the dynamic response. First, the Jacobian is constructed to determine the natural frequencies and stability of the equilibrium points shown in Fig. 12. The negative sign of the real part of the eigenvalue for the Jacobian reveals

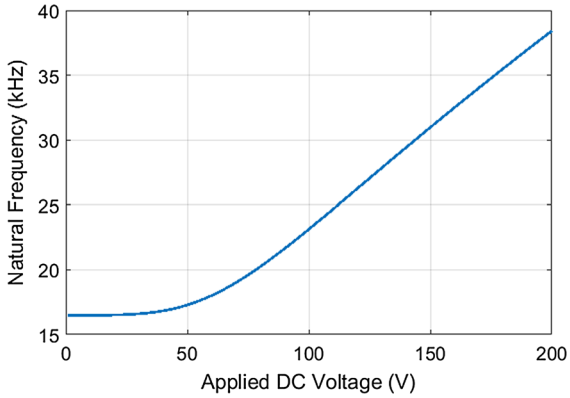


**Fig. 13** First natural frequency of the clamped–clamped beam as a function of DC voltage

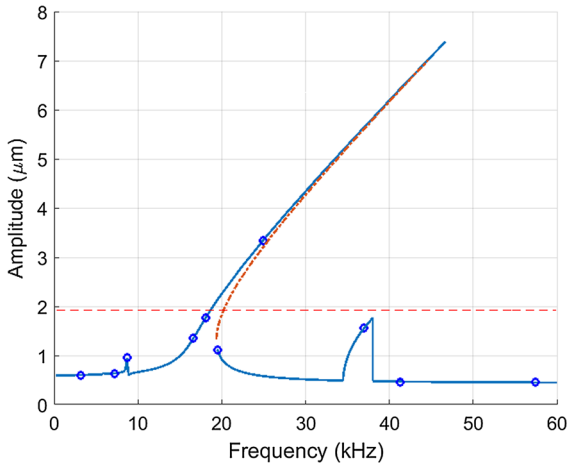


**Fig. 14** Frequency response at $V_{DC} = 50\,V$ and $V_{AC} = 10\,V$ from shooting method with one-mode approximation. *Markers* indicate two-mode approximations obtained from long-time integration

the equilibrium points are stable. The natural frequencies (the imaginary part of the eigenvalues) are depicted in Fig. 13.

Like with the cantilever beam, the natural frequency does not change much at low DC voltages but begins to increase linearly after approximately 55 V. In contrast, the clamped–clamped beam allows for much more control of the natural frequency. At 200 V, the natural frequency is increased by over 100%, as compared to 20% for the cantilever beam.

After the natural frequencies are computed, the steady-state response is determined using the shooting method as described in Sect. 3.1.2 with $\gamma = -1$, for one mode. Figures 14 and 15 show the frequency

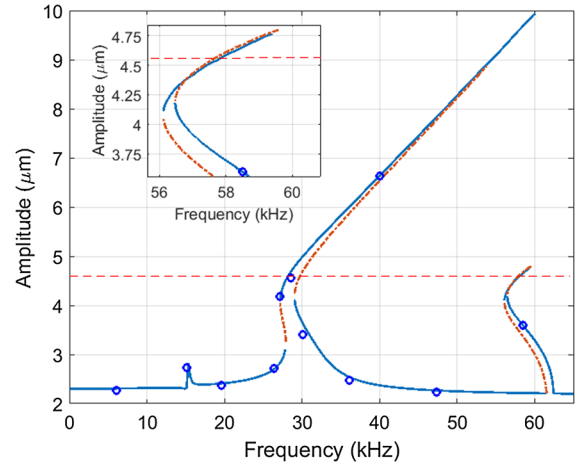


**Fig. 15** Frequency response at $V_{DC} = 150\,V$ and $V_{AC} = 10\,V$ from shooting method with one-mode approximation. *Markers* indicate two-mode approximations obtained from long-time integration. *Inlet* shows bifurcation in the subharmonic resonance

responses at $V_{DC} = 50\,V$ and $V_{AC} = 10\,V$, and $V_{DC} = 150\,V$ and $V_{AC} = 10\,V$, respectively. Blue solid lines represent the stable solution, and the orange dashed line indicates unstable solutions. The straight dashed line indicates the approximate threshold amplitude at which the beam will hit the electrode. The damping is estimated using Eq. (9) with a quality factor of 130. In these cases, larger AC voltages have been selected to investigate the nonlinear behavior of the system knowing that the system responds linearly to small AC excitation levels.

The system shows combined behavior because of the presence of quadratic and cubic nonlinearities. As shown in Fig. 14, at a lower excitation level of $V_{DC} = 50\,V$ and $V_{AC} = 10\,V$, the frequency bending of the system is dominated by the hardening effect from the nonlinearity of mid-plane stretching, which is a positive cubic nonlinearity. One can also observe subharmonic and super-harmonic resonances occurring at double and half of the resonance frequencies, which arise from the quadratic nonlinearity in the system.

As the voltage level is increased to $V_{DC} = 150\,V$ and $V_{AC} = 10\,V$ in Fig. 15, one can see the system shows mixed softening and hardening behavior in both primary and secondary resonances. Softening is caused by the quadratic and negative cubic term from the electrostatic force, while hardening occurs from the positive cubic term of the mid-plane stretching effect. We observed the negative cubic term ($p_3$)

of the forcing coefficients in Table 1 for the clamped–clamped beam turns to a positive cubic term from the mid-plane stretching effect, which, combined with the quadratic term, creates the mixed behavior. The mixed phenomenon of softening and hardening also has been reported in other research investigating nonlinear dynamics of clamped–clamped beams [43,44]. The unstable branches that appear because of nonlinearity in the system are effectively captured by the shooting method. However, the basin of attractions for some branches is very small. To capture the unstable solutions, we started from bifurcation points and increased the initial conditions by a very small amount to catch the unstable solution at the next frequency on the unstable branch. It is noted that some part of the high branch of the hardening response is above the threshold distance and thus not physically achievable.

There is also a cyclic fold bifurcation, where stable and unstable branches coalesce, in the subharmonic resonance at approximately 56 kHz. This arises from the mixed softening–hardening behavior of the resonator. At high voltages and low amplitudes, the subharmonic resonance is dominated by the softening nonlinearity from the electrostatic force. However, as the amplitude increases, mid-plane stretching becomes significant and hardening dominates.

The results of the shooting method using one mode are verified by checking the solution from long-time integration with two modes (one and three) on several points. As it can be seen in Figs. 14 and 15, there is a good agreement between the two, which validates the shooting method and the one-mode approximation. Two more indications that the solution is correct are that the static solution is close to the dynamic response at low frequencies and the resonant frequency is like what was predicted in Fig. 13. It should be mentioned that the results shown by blue circles over and above the threshold line are obtained by plugging in high initial conditions for the system. Such a high energy might be placed on the system by means of a mechanical shock. But as long as there is no source for high initial conditions, the system would remain below the threshold line, thus would not hit the substrate.

## 4 Conclusion

In this paper, a comprehensive study of static and dynamic responses of an electrostatic microbeam under the influence of a repulsive force is presented. A cantilever and a clamped–clamped beam are considered. This repulsive force is more appropriate for many optical and sensor-based applications because of its large out-of-plane stroke and the elimination of the pull-in instability, which is a severe limitation for electrostatic actuation.

As the applied force on the beam is pushing away from the substrate, we can obtain large travel ranges with a large DC and small AC voltages. For example, in the case of a 500-μm-long cantilever beam, dynamic amplitudes as high as 15 μm can be achieved with DC voltage of about 200 V and less than 1 V AC, while the initial gap is only 2 microns. A major drawback to this design is the large DC voltage required to place the static equilibrium point far away from the substrate to allow a large oscillation range. Even though, as seen in the experiment, voltages as high as 200 V can be applied to the devices without failure, getting 200 V in a practical application may be difficult. The cantilever also shows significant softening behavior. This is from the quadratic and negative cubic nonlinearity from the repulsive force. The experimental data verified these findings.

The clamped–clamped beam, on the other hand, is less likely to hit the bottom electrode because of strong restoring force caused by mid-plane stretching. The beam requires higher AC voltages to cause nonlinearities and broader frequency bandwidths compared to the cantilever. At very low voltages, the system behavior is linear. Increasing the voltage, strong hardening behavior appears. This is because of the positive cubic nonlinearity that stems from the mid-plane stretching term. Upon further increase of the voltage, the clamped–clamped beam shows a mixed softening and hardening behavior, although the hardening response dominates at large amplitudes. The analysis of the complex behavior of beams provides a framework for the application of electrostatic microbeams actuated by the repulsive force. This has a great potential to improve new generations of sensors and actuators that otherwise would have a limited range of motion caused by pull-in instability.

**Acknowledgements** The authors would like to thank the Binghamton Analytical and Diagnostics Laboratory for a small grant to use their equipment during static testing. We would also like to thank Dr. Ronald Miles and Dr. Abdallah Ramini for their help with the dynamic testing. Partial support for this study was provided by NSF ECCS Grant 1608692.

## Appendix

### Harmonic balance

In addition to the numerical shooting technique, an analytical method of harmonic balance was also used to verify the shooting method results. A steady-state solution is assumed in the form of a Fourier series. This is plugged into the governing differential equation and coefficients of the harmonic terms are equated. This results in a coupled set of algebraic equations that can be solved numerically [45]. The steady-state solution of Eq. (5) is assumed to be in the form

$$q(t) = a_0 + \sum_{j=1}^{N} a_j \sin(j\omega t) + b_j \cos(j\omega t) \tag{12}$$

where $a_j$ and $b_j$ are constants, and $N$ is the number of harmonics to be considered. For the cantilever, good convergence occurs at two harmonics and above. If the AC voltage is low enough that the frequency response looks approximately linear, one harmonic provides a good estimate of the solution. However, if the AC voltage is high enough to produce significant softening, at least two harmonics are necessary for an accurate solution in the region of the resonant peak. It should also be noted that only one mode is to be considered for the harmonic balance calculation.

Equation (12) is then plugged into Eq. (5), and the coefficients of the harmonic terms, as well as the remaining non-harmonic terms, are equated. The non-harmonic terms solve for the static solution of Eq. (5), while the harmonic terms determine the dynamic solution. This procedure is performed using Mathematica.

Because the forcing function is a 5th-order polynomial, the coupled algebraic equations for $a_j$ and $b_j$ are nonlinear and are difficult to solve analytically. Therefore, the Newton–Raphson method is employed. Once $a_j$ and $b_j$ are known, the maximum steady-state amplitude can be obtained by the relation shown in Eq. (13),

$$W = a_0 + \sum_{j=1}^{n} \sqrt{{a_j}^2 + {b_j}^2} \tag{13}$$

Figure 16 shows the comparison between the shooting and harmonic balance methods (2 harmonics) for the case of $V_{DC} = 195$ V and $V_{AC} = 1$ V with largest softening behavior in Fig. 6. The two results are in close agreement. It is noted that the harmonic balance method also yields a similar softening behavior.

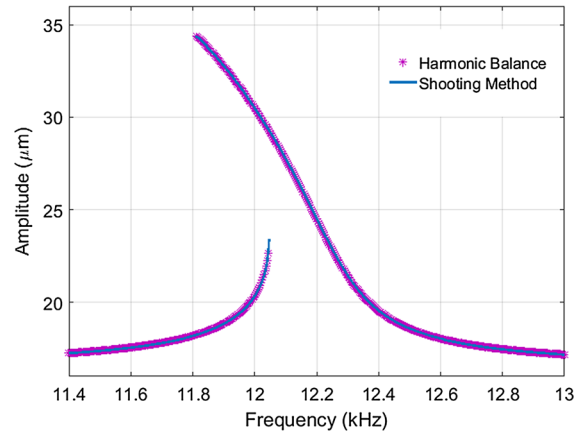


**Fig. 16** Comparison between shooting method and harmonic balance (2 harmonics) for one mode at $V_{DC} = 195$ V and $V_{AC} = 1$ V

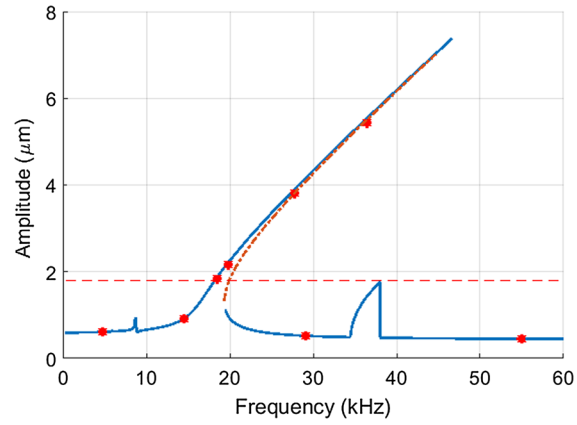


**Fig. 17** Frequency response at $V_{DC} = 50$ V and $V_{AC} = 10$ V with shooting method (1 mode). The *black solid line* represents the stable solution. *Markers* indicate results from harmonic balance method with one harmonic term

Next, this process is repeated for the clamped–clamped beam. Figure 17 depicts the comparison between the harmonic balance and shooting method results showing close agreement. For this case, only one harmonic is needed to show good agreement with the shooting method results.

## References

1. Davis, Z.J., Svendsen, W., Boisen, A.: Design, fabrication and testing of a novel MEMS resonator for mass sensing applications. Microelectron. Eng. **84**(5–8), 1601–1605 (2007)

2. Zhang, W.-M., Meng, G.: Nonlinear dynamic analysis of electrostatically actuated resonant MEMS sensors under parametric excitation. IEEE Sens. J. **7**(3), 370–380 (2007)
3. Harish, K.M., Gallacher, B.J., Burdess, J.S., Neasham, J.A.: Experimental investigation of parametric and externally forced motion in resonant MEMS sensors. J. Micromech. Microeng. **19**(1), 015021 (2008)
4. Chuang, C.-T., Chen, R.: Design, fabrication, and characterization of out-of-plane W-form microsprings for vertical comb electrodes capacitive sensor. J. Micro/Nanolithography MEMS MOEMS **8**(3), 033021 (2009)
5. Hu, Z., Gallacher, B.J., Harish, K.M., Burdess, J.S.: An experimental study of high gain parametric amplification in MEMS. Sens. Actuators A Phys. **162**(2), 145–154 (2010)
6. Frangi, A., Laghi, G., Langfelder, G., Minotti, P., Zerbini, S.: Optimization of sensing stators in capacitive MEMS operating at resonance. J. Microelectromech. Syst. **24**(4), 1077–1084 (2015)
7. Sharma, M., Sarraf, E.H., Cretu, E.: Shaped combs and parametric amplification in inertial MEMS sensors. In: 2013 IEEE SENSORS, Baltimore, MD, 4 pages. (2013)
8. Jia, Y., Yan, J., Soga, K., Seshia, A.A.: Parametrically excited MEMS vibration energy harvesters with design approaches to overcome the initiation threshold amplitude. J. Micromech. Microeng. **23**(11), 114007 (2013)
9. Park, J.Y., Lee, Y.P.: Modeling and characterization of piezoelectric $d_{33}$-Mode MEMS energy harvester. J. Microelectromech. Syst. **19**(5), 1215–1222 (2010)
10. Jamain, U.M., Ibrahim, N.H., Ab Rahim, R.: Performance analysis of zinc oxide piezoelectric MEMS energy harvester. IEEE International Conference on Semiconductor Electronics, Proceedings, ICSE **4**, 263–266 (2014)
11. Saadon, S., Wahab, Y.: From Ambient Vibrations to Green Energy Source: MEMS Piezoelectric Energy Harvester for Low Frequency Application. In: 2015 IEEE Student Symposium in Biomedical Engineering & Sciences (ISSBES) pp. 59–63 (2015)
12. Huang, F., Fouladi, S., Mansour, R.: A novel MEMS-based tunable dielectric resonator filter. In: IEEE MTT-S International Microwave Symposium Digest, pp. 2–5 (2011)
13. Shen, S.-H., Young, S.-T.: Design and fabrication of a MEMS filter bank for hearing aids applications. In: Proceedings (Cat. No. 02EX578) 2nd Annual International IEEE-EMBS Special Topic Conference on Microtechnologies in Medicine and Biology, pp. 352–355 (2002)
14. Diamantis, S., Ahmadi, M., Jullien, G.A., Miller, W.C.: A Programmable MEMS bandpass filter. In: Proceedings of the 43rd IEEE Midwest Symposium on Circuits and Systems (Cat. No. CH37144), pp. 522–525 (2000)
15. Huang, J.M., Liu, A.Q., Deng, Z.L., Zhang, Q.X.: A modeling and analysis of spring-shaped torsion micromirrors for low-voltage applications. Int. J. Mech. Sci. **48**(6), 650–661 (2006)
16. Sharma, M., Sarraf, E.H., Cretu, E.: Parametric amplification/damping in MEMS gyroscopes. In: Proceedings of the IEEE International Conference on Micro Electro Mechanical Systems (MEMS), pp. 617–620 (2011)
17. Guo, C., Fedder, G.K.: Behavioral modeling of a CMOS-MEMS nonlinear parametric resonator. J. Microelectromech. Syst. **22**(6), 1447–1457 (2013)
18. Rabih, A.A.S., Dennis, J.O., Abdullah, M.A.: Design, Modeling and Simulation of CMOS–MEMS Resonator for Biomedical Application. In: 2014 5th International Conference on Intelligent and Advanced Systems (ICIAS), pp. 4–9 (2014)
19. Rebeiz, G.M.: RF MEMS: Theory, Design, and Technology. Wiley, New York (2003)
20. Nathanson, H.C., NewellW, E., Wickstrom, R.A., Davis, J.R.: The resonant gate transistor. IEEE Trans. Electron Devices **3**, 117–133 (1967)
21. Braghin, F., Resta, F., Leo, E., Spinola, G.: Nonlinear dynamics of vibrating MEMS. Sens. Actuators A Phys. **134**(1), 98–108 (2007)
22. Ruzziconi, L., Bataineh, A.M., Younis, M.I., Cui, W., Lenci, S.: Nonlinear dynamics of a MEMS resonator: theoretical and experimental investigation. AIP Conf. Proc. **1493**, 822–829 (2012)
23. Younis, M.I., Ouakad, H.M., Alsaleem, F.M., Miles, R., Cui, W.: Nonlinear dynamics of MEMS arches under harmonic electrostatic actuation. J. Microelectromech. Syst. **19**(3), 647–656 (2010)
24. Towfighian, S., Heppler, G.R., Abdel-Rahman, E.M.: Analysis of a chaotic electrostatic micro-oscillator. J. Comput. Nonlinear Dyn. **6**, 011001 (2011)
25. Ozdogan, M., Towfighian, S.: Nonlinear dynamic behavior of a bi-axial torsional MEMS mirror with sidewall electrodes. Micromachines **7**(3), 42 (2016)
26. Towfighian, S., Seleim, A., Abdel-Rahman, E.M., Heppler, G.R.: A large-stroke electrostatic micro-actuator. J. Micromech. Microeng. **21**(7), 075023 (2011)
27. Elshurafa, A.M., Khirallah, K., Tawfik, H.H., Emira, A., Aziz, A.K.S.A., Sedky, S.M.: Nonlinear dynamics of spring softening and hardening in folded-mems comb drive resonators. J. Microelectromech. Syst. **20**(4), 943–958 (2011)
28. Lee, K.B., Cho, Y.H.: Laterally driven electrostatic repulsive-force microactuators using asymmetric field distribution. J. Microelectromech. Syst. **10**(1), 128–136 (2001)
29. Shen, N., Kan, E.C.: Novel electrostatic repulsion forces in MEMS applications by nonvolatile charge injection. In: Technical Digest. MEMS 2002 IEEE International Conference. Fifteenth IEEE International Conference on Micro Electro Mechanical Systems (Cat. No. 02CH37266), pp. 598–601 (2002)
30. He, S., Ben Mrad, R.: Large-stroke microelectrostatic actuators for vertical translation of micromirrors used in adaptive optics. IEEE Trans. Ind. Electron. **52**(4), 974–983 (2005)
31. Sugimoto, T., Nonaka, K., Horenstein, M.N.: Bidirectional electrostatic actuator operated with charge control. J. Microelectromech. Syst. **14**(4), 718–724 (2005)
32. He, S., Ben Mrad, R.: Development of a multi-level repulsive force out-of-plane micro electrostatic actuator. In: IECON Proceedings (Industrial Electronics Conference), pp. 4020–4023 (2009)
33. He, S., Ben Mrad, R.: Design, modeling, and demonstration of a MEMS repulsive-force out-of-plane electrostatic micro actuator. J. Microelectromech. Syst. **17**(3), 532–547 (2008)
34. Chong, J., He, S., Ben Mrad, R.: Control of a surface micromachined repulsive-force driven 2D micromirror. In: IEEE/ASME International Conference on Advanced Intelligent Mechatronics, AIM, pp. 1005–1007 (2010)

35. Fan, C., He, S.: A two-row interdigitating-finger repulsive-torque electrostatic actuator and its application to micromirror vector display. J. Microelectromech. Syst. **24**(6), 2049–2061 (2015)
36. Li, G., Guo, X., Zhao, Q., Hu, J.: An Electrostatic Repulsive-Force Based Micro Actuator for Capacitive RF MEMS Switch, pp. 1095–1098 (2015)
37. Qiao, D.Y., Yuan, W.Z., Li, X.Y.: Design of an electrostatic repulsive-force based vertical micro actuator. In: Proceedings of 1st IEEE International Conference on Nano Micro Engineered and Molecular Systems, 1st IEEE-NEMS, vol. 90407020, pp. 168–171 (2006)
38. Younis, M.I.: MEMS Linear and Nonlinear Statics and Dynamics. Springer, New York (2011)
39. Rao, S.S.: Mechanical Vibrations, 5th edn. Prentice Hall, Upper Saddle River, NJ (2011)
40. Nayfeh, A.H., Balachandran, B.: Applied Nonlinear Dynamics: Analytical, Computational, and Experimental Methods. John Wiley & Sons, New York (1995)
41. Jaber, N., Ramini, A., Carreno, A.A.A., Younis, M.I.: Higher order modes excitation of electrostatically actuated clampedclamped microbeams: experimental and analytical investigation. J. Micromech. Microeng. **26**(2), 025008 (2016)
42. Younis, M.I., Abdel-Rahman, E.M., Nayfeh, A.: A reduced-order model for electrically actuated microbeam-based MEMS. J. Microelectromech. Syst. **12**(5), 672–680 (2003)
43. Ramini, R.H., Hennawi, Q.M., Younis, M.I.: Theoretical and experimental investigation of the nonlinear behavior of an electrically actuated in-plane MEMS arch. J. Microelectromech. Syst. **25**(3), 570–578 (2016)
44. Ouakad, H.M., Younis, M.I.: Nonlinear dynamics of electrically actuated carbon nanotube resonators. J. Comput. Nonlinear Dyn. **5**(1), 011009 (2010)
45. Nayfeh, A.H., Mook, D.T.: Nonlinear Oscillations. Wiley, New York (1979)